



HISTO - MRI

This project has received funding from the European Union's H2020 Programme under grant agreement no 737180— HISTO-MRI

D2.3: Prototype of the full magnet system



| Version | Date | Reviewer |
|----------------|-------------|------------------|
| 1 | 07/02/2020 | Juan Pablo Rigla |
| 2 | 12/02/2020 | Joseba Alonso |



Table of contents

| | |
|----------------------------------------|----------|
| 1 Deliverable description | 4 |
| 2 Introduction..... | 4 |
| 2.1 Magnetic system. | 4 |
| 2.1.1 Main Magnet system..... | 4 |
| 2.1.2 Prepolarized Magnet system..... | 7 |
| 2.2 Gradient System. | 9 |
| 2.3 Radiofrequency System..... | 10 |

1 Deliverable description

This deliverable describes the main components of the HISTO - MRI equipment: Magnetic system (main and prepolarized magnets), gradient system and radiofrequency system. This deliverable is the results of *Task 1, 2 and 3* of **WP2**.

2 Introduction

The **HISTO-MRI** system will incorporate an innovative approach with the development of a novel high-field pre-polarized MRI (pMRI) magnet. This MRI scanner will employ two separate fields produced by two different magnets. A pulsed, strong and inhomogeneous magnetic field will be used to polarize the sample prior to imaging, in order to increase signal-to-noise ratio (SNR) in subsequent evolution images obtained at lower magnetic field strength. The **HISTO-MRI** system will incorporate ultra-steep and ultra-fast (rise time $\leq 10 \mu s$) magnetic gradients without peripheral nerve stimulation which, with the high SNR afforded by the pre-polarization approach, will result in significant improvements in spatial resolution and acquisition times as compared to existing MRI systems. The RF system will incorporate a transmit/receive coil operating at a frequency of 42.57 MHz, corresponding to the static homogeneous magnetic field strength of 1.0 Tesla.

2.1 Magnetic system.

2.1.1 Main Magnet system.

For the main magnetic field, B_0 , the main requirements to meet for the high resolution targeted in the HISTO – MRI project are a rampable magnetic field up to 1 T and a spatial homogeneity better than 100 ppm in a FoV defined by a spherical region of diameter 20mm.

To meet this goals, we have opted for an electromagnet with a classical “H” – shaped structure. This geometry allows higher magnetic field and offers greater mechanical stability than the “C” – shaped structures. This magnet has a gap, space free between magnetic poles, of 70 mm and a diameter poles of 250 mm. To improve the homogeneity of the magnetic field we opt for an alternative to the standard solution consisting of a thick iron shim placed at the pole edges (Rose – shim). Our alternative was to make profile – height variations $<100 \mu m$ in the magnetic poles. This alternative allowed us to obtain a magnetic field homogeneity of 71 ppm in the FoV¹.

In order to generate the field, the magnet counts with two circular coils of 156 turns each, with a

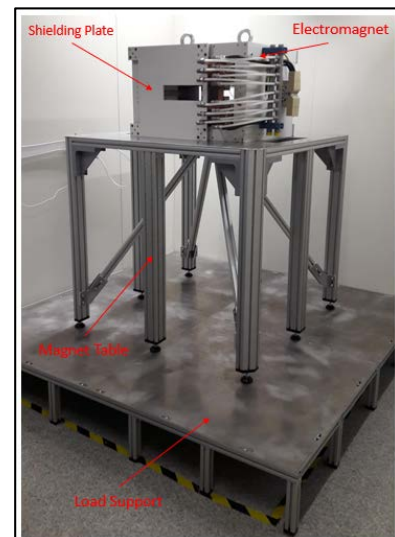


Figure 1: Picture of the HISTO – MRI system.

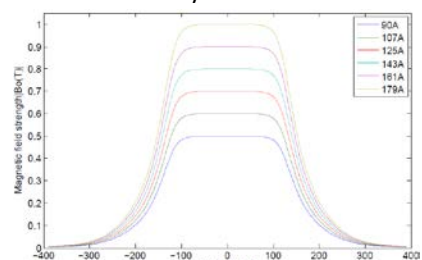


Figure 2: Z-axis distribution of the magnetic field magnitude $|B_0(z)|$ for maximal field strengths ranging from 0.5 to 1 T.

¹ J. P. Rigla *et al.*, "Low-Field Rampable Magnet for a High-Resolution MRI System," in *IEEE Transactions on Magnetics*, vol. 56, no. 2, pp. 1-7, Feb. 2020, Art no. 5100107. doi: 10.1109/TMAG.2019.2950891

total conductor cross section of 51 mm². With this design, a current of ≈ 180 A through the coils results in the desired maximal-field strength of 1 T (**Fig.2**). With this design the electromagnet has a total mass of 950 kg.

The presence of the electromagnet will result in unwanted and potentially dangerous effects on other components and laboratory equipment if the peripheral fringe field outside the core is sizable. Fringe fields are typically characterized by the extent of the 5 G surface. This surface reaches 610 mm from the front and back of the bare magnet if operated at 1 T, well beyond desired.

The solution we finally implemented compresses the magnetic field lines inside the magnet with two steel plates on its front and back (see **Fig.3**). After simulating a variety of arrangements, we opted for steel plates of 10mm thickness separated 20mm from the magnet faces. This results in a 5G surface just beyond the magnet outer walls. However, the extra weight from the steel plates forced us to redimension the yoke, whose length went from 200 to 270mm and whose thickness went from 90 to 67mm. In this final design, the 5G surface is confined to be <365mm from the magnet center and <65mm from its outer structure. The experimental characterization of the electromagnet indicates that the magnetic field homogeneity in the FoV is barely affected by the shield.

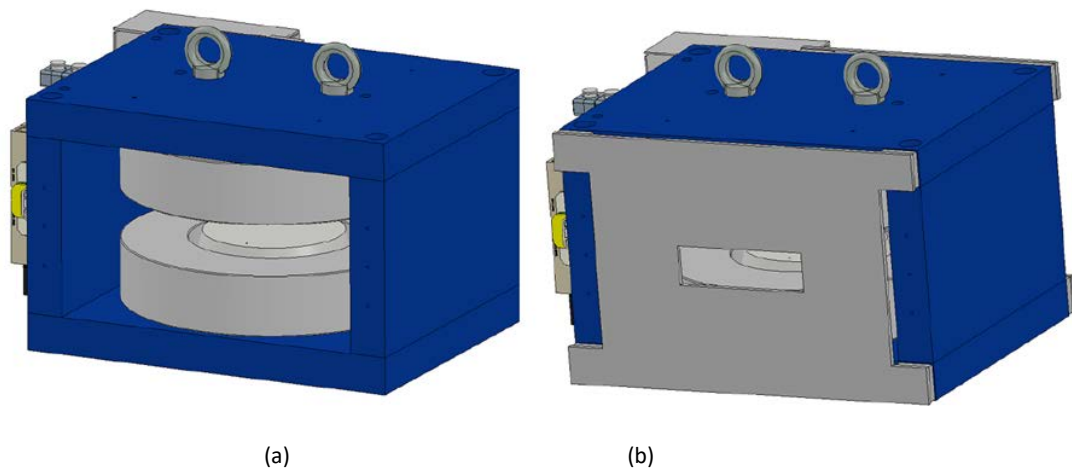


Figure 3: 3-D models of the magnet without (a) and with (b) shielding steel plates.

For the generation of the maximum magnetic field, the magnet requires currents up to 180A, leading to voltage drops of up to 30 V across the coils. Hence, up to 5.4 kW of power can be dissipated in the magnet structure. We have split each coil into four loops, with three layers per loop, to allow for efficient cooling. The thermal simulations that a water flow of 12 l/min and a drop pressure of 4 bar will limit the temperature increase at the coils to 6 K. This magnet uses a SMC HRS060 chiller cooling system.

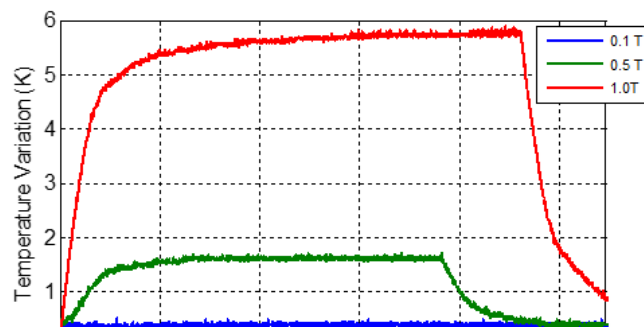


Figure 4: Temperature variation (K) as a function of the time (s) observed in the cooling system for three magnetic field values: 1T (blue line), 0.5 T (green line) and 0.1T (blue line). Temperature water input was 293K.

Monitoring of the water flow and temperature is realized by two flowmeters (SMC HRS-PF3W540) located at the input and exit of the electromagnet. The thermal evolution of the magnet for different current values is observed in **Fig.4**. The maximum temperature increase throughout the coil was observed in the cooling system for 1 T (186 A), 5.9 K and for 0.1 T (17.8 A) the jump is negligible.

The weight of the magnet imposes the use of a robust and reliable mechanical structure. To ensure the structural integrity of the system and the building, the load must be kept <350 kg/m² and the load distribution should be as uniform as possible. To avoid the strong forces between the support structure and the magnet, we built the former out of aluminum 6063. The mechanical structure of the magnet is formed by two components: the magnet table and the load support. A photograph of the electromagnet with the mechanical support mounted in the MRILab at the i3M is shown in **Fig.1**.

We have characterized the spatial field-strength distribution and overall performance of the main magnet with a Hall probe attached to a 3-D positioning system. The positioners in the transverse (vertical) directions move in a range of up to 500mm and are accurate at the 100 μm level, whereas the Hall probe is specified to have an accuracy of 0.1 mT with the settings used in most measurements. For these tests, we supplied current to the magnet with a Danfysik 9100 Unipolar Power Supply.

The magnetic-field strength measured along the Z-axis closely resembles that expected from electromagnetic simulations (**Fig.5, left**). We have also measured the field with and without the magnetic shield to characterize its influence on the position of the 5G line and the homogeneity in the FoV (**Fig.5, right**). These measurements indicate that the 5 G fringe-field limit for the magnet without the shield lies ≈ 430mm from the magnet center (≈ 130mm from the outer surface), while placing the shield brings it down to ≈ 325mm, in agreement with simulations. The effect of the shield on the field distribution in the FoV was imperceptible.

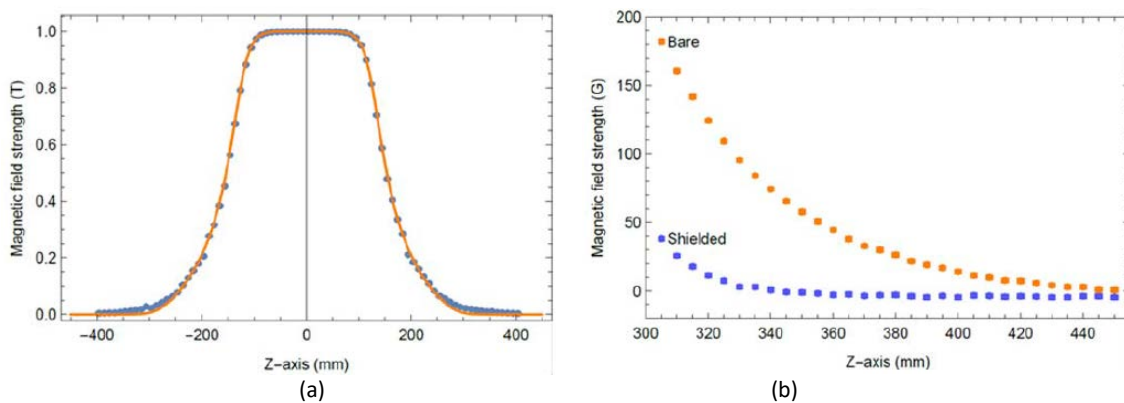


Figure 5: Magnetic-field profile along the Z-axis for $B_0 \approx 1\text{ T}$ for electromagnetic simulations (solid, orange line) and experimental measurements (blue points) (a). Fringe-field measurements along the Z-axis for a maximal field strength of 1 T for the final magnet design with and without the shielding (b). Error bars are partly hidden behind the points.

For the experimental characterization, we scanned a cubic volume of sides 20 mm and we obtained an experimental homogeneity of ≈ 71 ppm, very close to the simulated value (≈ 68 ppm). Deviations from the nominal B_0 along the three Cartesian axes can be read in **Fig.6**.

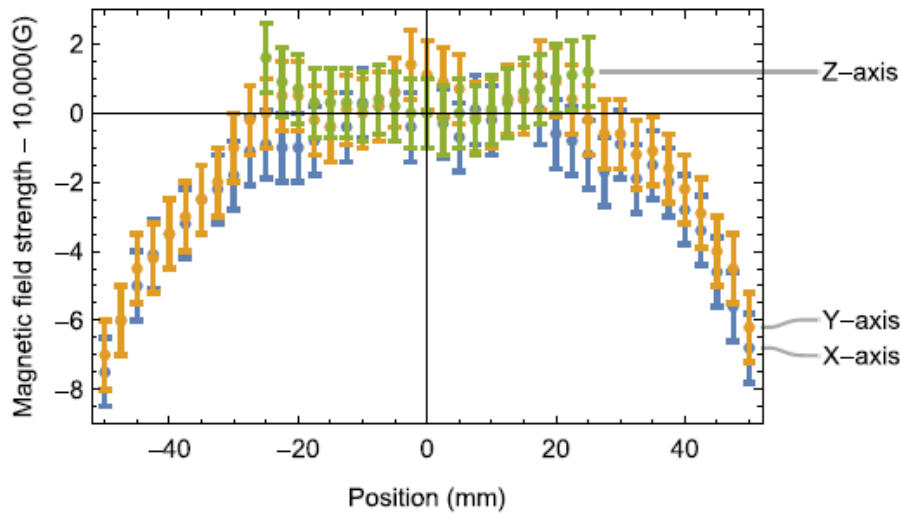
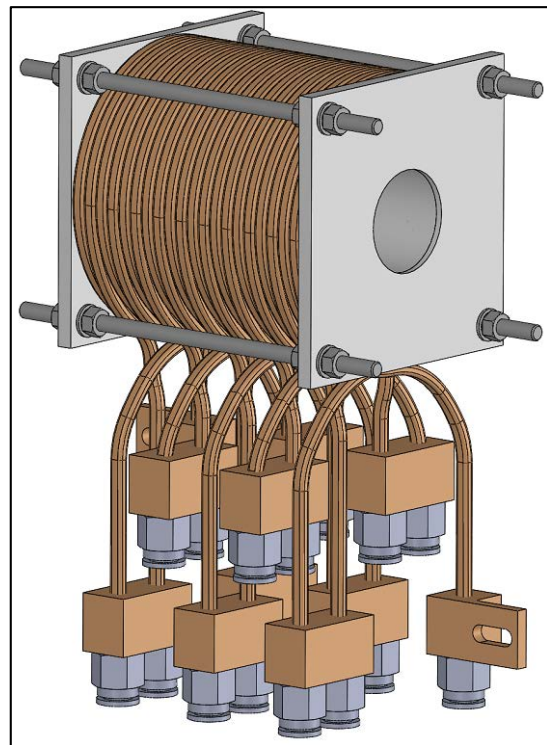


Figure 6: Magnetic-field strength along the X- (blue), Y- (yellow), and Z (green)-axes for $B_0 \approx 1$ T.

2.1.2 Prepolarized Magnet system.

For the prepolarizer magnet design was taken into account that this magnet will have to generate a magnetic field greater than 0.5 T. For the final design, the magnet consists of ten loops, two layers per loop (spiral configuration), with a sixteen turns per loop. The electric conductor used is the same as in the previous designs. A 3D CAD model of the prepolarizer magnet is shown in **Fig.7**. The loops are electrically connected in series and the water cooling paths are connected in parallel to maximize heat transfer. For manufacture the prepolarizer magnet, the conductive material selected was a special OF-OK Copper hollow conductor. The hollow tube has a 4×3 mm² copper section and an inner hole of 2 mm in diameter where the coolant (water) of the cooling system will circulate.



A current of 280 A is necessary to generate the desired magnetic field, 0.5 T. Thermal simulations indicate that a water flow of 13.43 l/min and a drop pressure of 4 bar will limit the temperature increase at the coils to 12.5 K in the magnet.

The prepolarizer magnet was manufactured by ANTEC² (Portugalete, Spain) and the magnetic characterization of the prepolarizer magnet was carried at MRILab (i3M, Spain). This characterization was carried out using a magnetic test bench. This test bench has a Hall sensor attached to a 3D positioning system. A picture of the prepolarizer magnet during the experimental characterization is shown in **Fig.8**. The magnetic characterization of this magnet was performed in DC (maximum current 200 A) using the Danfysik 9100 Unipolar Power Supply. This power supply is used to supply the power to the main magnet of the HISTO-MRI system. The prepolarized magnet was cooled using a SMC HRS-090 chiller.



Figure 8: Picture of the Prepolarizer magnet during the experimental characterization at MRILab (i3M).

The magnetic properties of the prepolarizer magnet were studied along the X – axis (distance equal to 160 mm), central axis of the magnet. The magnetic field measurements were taken every 2.0 mm. The magnetic field profiles along the X – axes ($Z=Y=0$) for different currents (I_{max} equal to 190 A) are shown in **Fig.9**.

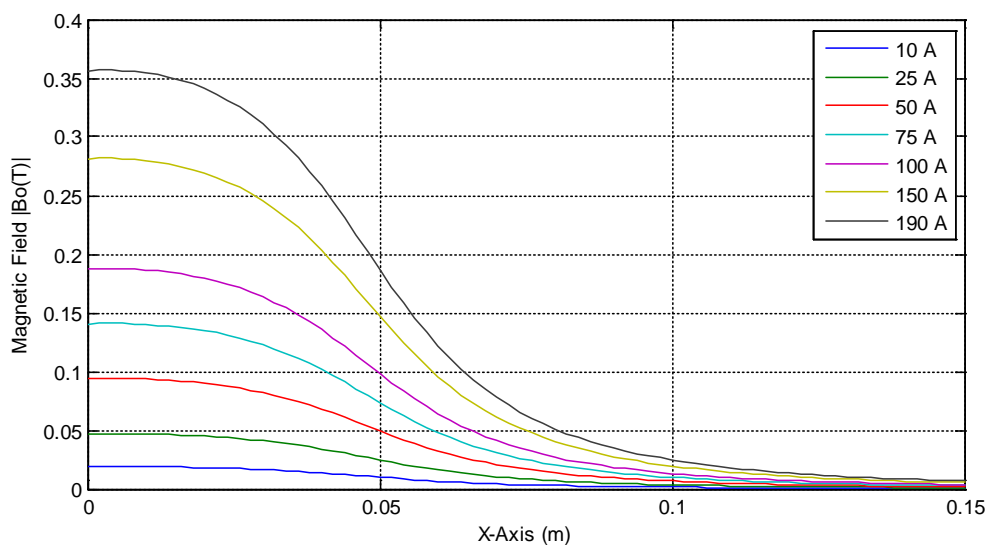


Figure 9: Distribution of the magnetic field $|B_0(z)|$ for different currents along to the X- axis.

² <https://antec-group.com/magnets/>

2.2 Gradient System.

The HISTO-MRI system incorporate strong (1.2 T/m) and ultra-fast (rise time $\leq 10 \mu\text{s}$) magnetic gradients without peripheral nerve stimulation which, with the high SNR afforded by the pre-polarization approach, will result in significant improvements in spatial resolution and acquisition times as compared to existing MRI systems. These ultra-steep and ultra-fast magnetic field gradients will assist in avoiding distortions due to local magnetic field in-homogeneities and will allow extremely high spatial resolution ($\leq 20 \mu\text{m}$).

For the design of the coils we took into account that these coils should have the minimum possible inductance to be able to reach the rise and fall times $\leq 10 \mu\text{s}$ and the minimum possible resistance to be able to withstand the high currents (500 A) that will circulate at through them. Taking these two conditions into account we have designed a planar and open gradient system composed of six planar coils³. The manufacturing the coils was made from a conductive material used is a special OF-OK Copper hollow conductor provided by Luvata (same conductor used to make the prepolarizer magnet), typically used in applications where high electrical and thermal conductivity are required, as is the present application. Also, connection hub was designed and manufactured and also welded to the gradient coils. The connection hub connects both electric and hydraulic systems with the gradient coils. The dimensions of the selected hollow tube, connection hub and the used fittings and a total gradient coil is shown in **Fig.10**. A dielectric structure (see **Fig.11**) manufactured by sintering polyamide is use to fix gradient coils.

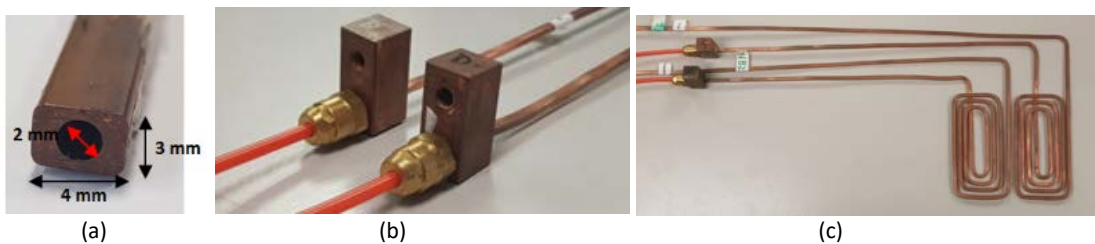


Figure 10: Cross section hollow tube (a), hydraulic and electric fitting coils (b). Final gradient coil manufactured (c).



Figure 11: Gradient polyamide structure. Y-coil layer (left). Final assembly (right).

The gradient coils have been magnetically characterized by studying the gradient magnetic field and also the resistance and inductance values at different frequency ranges once built (see **Fig.12, right**), before installing them inside the main magnet. The expected gradient field

³ D. Grau et al., *Patent Application* US P201830448 (2018).

by using an intensity current of $I = 400 \text{ A}$ is $G_x = 1.7 \text{ T/m}$. Experimental measurements confirm the performed simulations (**Fig.12, left**).

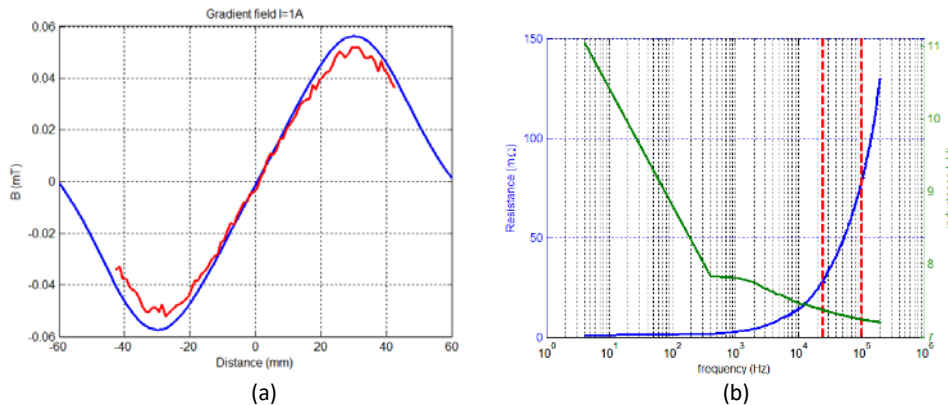


Figure 12: Magnetic profile by using an intensity current $I=1\text{A}$. Blue line: expected values, red line: experimental values (a). X-coil set axis resistance and inductance experimental values in a frequency range between 4Hz and 200 kHz (b).

In order to use a high intensity current, it is necessary to refrigerate each of the coils. This is done using a pump and cooler that provide a constant flow to the entire hydraulic system, SMC HRS-090 chiller. Preliminary simulations show a temperature increase lower than 12.5°C when a DC intensity current of $I=400\text{A}$ is used.

2.3 Radiofrequency System.

For the radiofrequency setup we use a loop gap resonator (LGR). The LGR is composed of a copper cylinder with a longitudinal gap (see **Fig.13a**). The fabricated LGR diameter is 15 mm and its length is 50 mm. The LGR coil is covered by an external cylindrical shielding (see **Fig.13b**), whose diameter and length are 21 mm and 100 mm, respectively. We fabricated the housing with poly lactic acid (PLA) which can be easily synthesized by 3D printing and had a good mechanical resistance to support the weight of the hole subsystem. We include in the housing a plug to fit into the actuator that moves the hole system in and out the magnet. The first advantage of the LGR is its short electric length (4.7 cm), which is much shorter than the tenth of the wavelength ($\lambda/10 = 70 \text{ cm}$). For this reason, we do not need any capacitor along the RF coil. The second advantage is its low inductance and high capacitance, which results in a low electric field around the coil, reducing the effect of the sample on the RF coil impedance.

Currently, we tune the coil to 42.6 MHz (i.e. Larmor frequency corresponding to a static magnetic field of 1 T) and match its impedance to 50 Ohms by means of a conventional tuning/matching circuit consisting of fixed and trimmer capacitors. However, this conventional circuit does not allow for automatic tuning/matching. Automatic tuning/matching can be helpful to ensure an optimal RF coil performance along the acquisition. Our first approach to do automatic tuning/matching was by means of varactor diodes (**Fig.14a**). Varactor diodes are diodes designed to exploit the voltage-dependent capacitance of a reverse-biased diode. This should allow us to control the tuning or matching capacitance through DC voltage. However, while this method is useful for low power signal (e.g. in just receiving RF coils), high RF power used in the transmission affects varactor diodes capacitance significantly in each signal cycle, giving rise to a time-varying capacitance. To overcome this inconvenient, we are currently working on a different matching network based on capacitor networks activated by diodes (**Fig.14b**). For each

tuning or matching capacitor, we add additional capacitance by driving forward a PIN diode series connected to a capacitor. In this way, we can control the total capacitance with a resolution given by the smallest capacitor in the network.

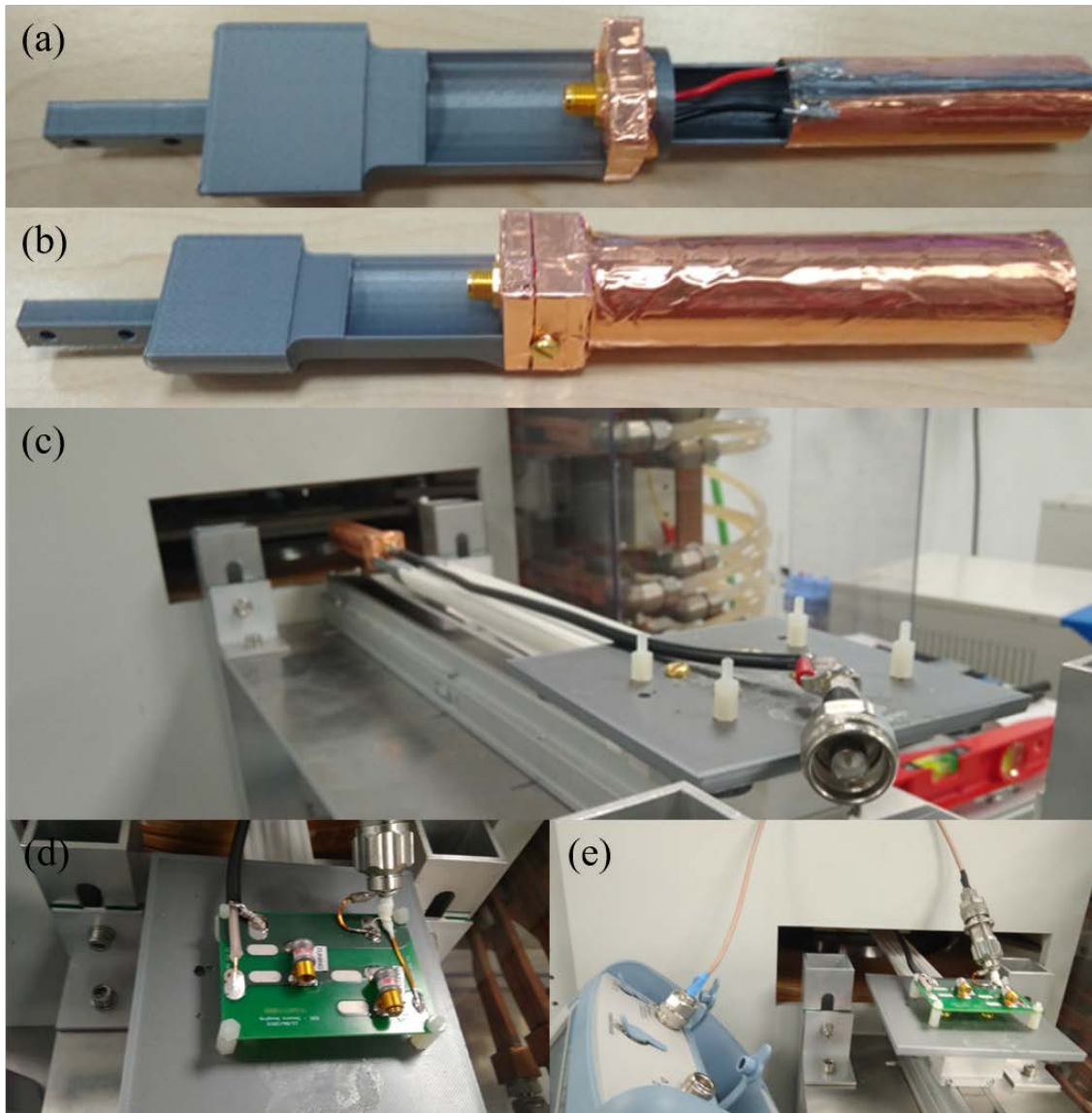


Figure 13: Pictures of (a) the LGR coil, (b) the LGR shielding, (c) the LGR coil in the actuator inside the magnet (d) and (e) the matching network when the LGR is fully inside the magnet

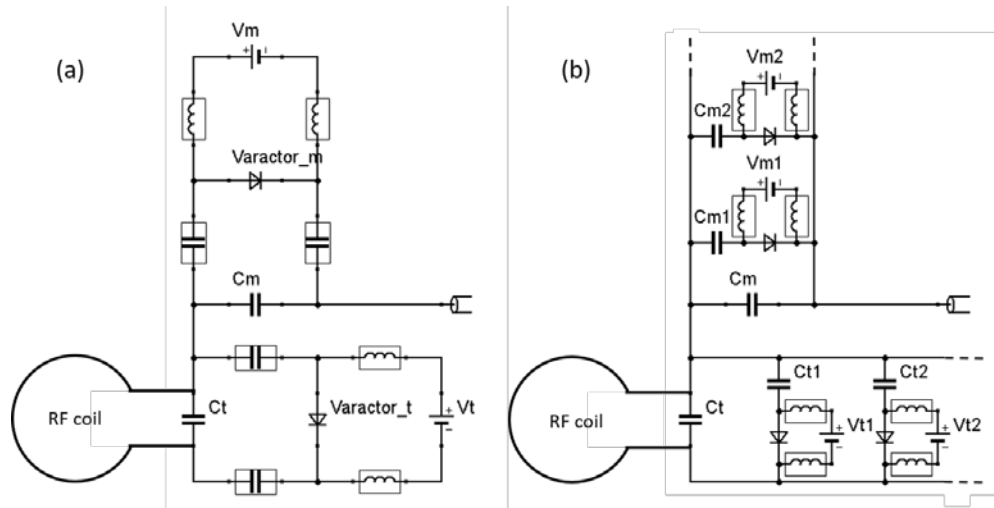


Figure 14: (a) Voltage controlled matching network by means of varactor diodes. (b) Voltage controlled matching network by means of capacitor network with diodes.

In addition to the RF coil subsystem, we have the hole RF setup ready for use. This includes basically three different devices: RF power amplifier, preamplifier and TxRx switch (**Fig.15a**). We purchased the high power electronics from Barthel HF-Technik. The RF power amplifier (RFPA-42-1000, Barthel HF-Technik) will input high power RF signal to the LGR coil. This RF signal is necessary to produce oscillating magnetic field that will excite the sample. Because the LGR coil will work as a TxRx coil, we need to include in the RF electronics a TxRx switch (RXTX42, Barthel HF-Technik). The purpose of the TxRx switch is to protect the receiving preamplifier from the damage due to high RF power of transmit mode. Finally, we got a 50 Ohms input impedance preamplifier (LNA01, Barthel HF-Technik) to amplify the weak received signal from proton magnetic resonance. We also need to pay special attention to reduce shield currents or common mode currents along the coaxial cable. Shield currents affect coil tuning, image inhomogeneity and, most importantly, can cause serious burns. Shield currents are reduced by cable traps; they consist of a wound coaxial cable inductor tuned to the desired resonance frequency by a capacitor between the turns of the coaxial cable ground shield. However, in this case we have decided to use floating cable traps (**Fig.15b**), which do not connect or solder to the cable itself and can be split, allowing easy fitting over any cable. The floating cable trap consists of two coaxial concentric conductive cylinders, where one end is shorted together and the other end is tuned to resonance. This essentially creates and tunes LC tank circuit. We designed a cable trap with 2.5 cm outer diameter, 0.7 cm inner diameter, 10 cm length and tuning capacitor of 516 pF. The cable trap was measured to reject the common mode with a total attenuation of -8 dB.

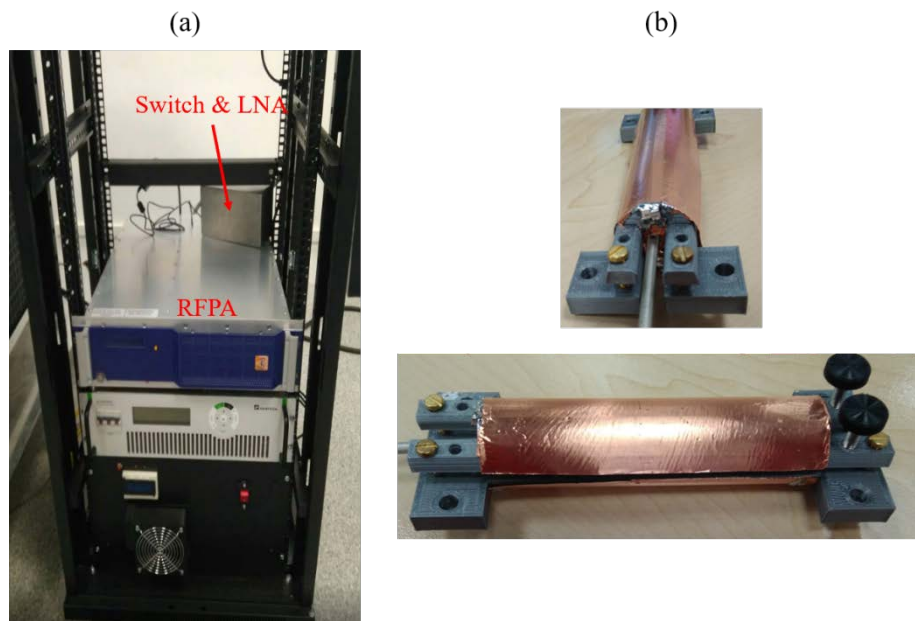


Figure 15: (a) Picture of the radiofrequency power amplifier together with the switch and the low-noise amplifier (both in the same box). (b) Pictures of the floating cable trap fabricated to reject the common mode along the coaxial cables.